

# Fast water transport in graphene nanofluidic channels

Quan Xie<sup>1</sup>, Mohammad Amin Alibakhshi<sup>1</sup>, Shuping Jiao<sup>2</sup>, Zhiping Xu<sup>2</sup>, Marek Hempel<sup>3</sup>, Jing Kong<sup>3</sup>, Hyung Gyu Park<sup>4</sup> and Chuanhua Duan<sup>1\*</sup>

**Superfast water transport discovered in graphitic nanoconduits, including carbon nanotubes and graphene nanochannels, implicates crucial applications in separation processes and energy conversion. Yet lack of complete understanding at the single-conduit level limits development of new carbon nanofluidic structures and devices with desired transport properties for practical applications. Here, we show that the hydraulic resistance and slippage of single graphene nanochannels can be accurately determined using capillary flow and a novel hybrid nanochannel design without estimating the capillary pressure. Our results reveal that the slip length of graphene in the graphene nanochannels is around 16 nm, albeit with a large variation from 0 to 200 nm regardless of the channel height. We corroborate this finding with molecular dynamics simulation results, which indicate that this wide distribution of the slip length is due to the surface charge of graphene as well as the interaction between graphene and its silica substrate.**

Superfast water transport has been discovered in graphitic nanoconduits<sup>1,2</sup> (for example, carbon nanotubes (CNTs) and graphene nanochannels) and their membrane forms<sup>3–5</sup> (for example, CNT membranes and graphene oxide membranes) and has inspired great interest for applications in water desalination<sup>6–9</sup>, nanofiltration<sup>10–12</sup>, energy harvesting<sup>13,14</sup> and lab-on-a-chip<sup>15,16</sup>. Further development and application of these carbon nanofluidic structures rely on accurate measurement and understanding of water flow enhancement and surface slippage as a function of confinement, curvature and surface properties down to the level of single conduits. Although great progress has been made exploring water transport and diameter-dependent slippage in single CNTs<sup>17,18</sup>, water transport in single graphene nanochannels, which is ideal for lab-on-a-chip applications<sup>15</sup> and is the basic unit of graphene oxide membranes<sup>5,19–21</sup>, has yet to be unambiguously studied.

There are a number of challenges for water transport study in single graphene nanochannels, which to some extent are more difficult to overcome than those in single CNTs<sup>18</sup>. First, single graphene nanochannels with well-controlled dimensions and atomically smooth graphene surfaces need to be fabricated on the target substrate using facile fabrication methods. Second, ultra-low flow rate due to nanoconfinement and the corresponding pressure difference across the single graphene nanochannel need to be precisely measured without using any theoretical estimation. So far, there have been only limited efforts to resolve these two challenges. Graphene nanochannels down to 0.7 nm were created using multi-layer graphene as the spacer layer and water transport across these was studied by measuring liquid-transport-limited evaporation at the nanochannel entrances<sup>5</sup>. However, the fabrication method lacked precise control over the channel length and the driving pressure of water flow was estimated by molecular dynamics (MD) simulation, whose accuracy has yet to be validated. Recently, we developed a new method to construct graphene nanochannels with well-controlled geometries to investigate enhanced ion transport<sup>15</sup>.

In this work, we employ the same method to fabricate graphene nanochannels with three-side graphene coverage to overcome the first challenge. For the second challenge, we use capillary flow to optically measure the flow rate in individual graphene nanochannels while employing a hybrid nanochannel design to avoid inaccurate estimation of the driving pressure<sup>22</sup>.

## Hybrid nanochannel design

As shown in Fig. 1a,b, the hybrid nanochannel consists of a graphene nanochannel connected with a silica nanochannel that has the same height and width. The graphene nanochannel is the channel to be investigated, and the silica nanochannel serves as the reference nanochannel whose hydraulic resistance (permeability) is known<sup>22</sup>. Both ends of the hybrid nanochannel (the graphene end and the silica end) are open to allow water introduction for capillary filling. In a typical experiment, two capillary flow measurements are conducted in the hybrid channel, one starting from the graphene side and the other starting from the silica side. The meniscus positions in the graphene channel,  $X_1(t)$  and  $X_2(t)$ , for these two capillary measurements are expected to follow the two equations below (see Supplementary Section 1):

$$X_1(t)^2 = 2At \quad (1)$$

$$X_2(t)^2 + 2\beta LX_2(t) = 2At \quad (2)$$

Here,  $t=0$  is the time at which the meniscus enters the graphene channel,  $A$  is the capillary flow constant of the graphene channel, which entails the mass flow resistance and the capillary pressure terms,  $L$  represents the length of the silica nanochannel, and  $\beta = \frac{R_s}{R_G}$  is the ratio of the mass flow resistance per unit length between silica nanochannel ( $R_s$ ) and graphene nanochannel ( $R_G$ ).

<sup>1</sup>Department of Mechanical Engineering, Boston University, Boston, MA, USA. <sup>2</sup>Department of Engineering Mechanics and Center for Nano and Micro Mechanics, Tsinghua University, Beijing, China. <sup>3</sup>Department of Electrical Engineering and Computer Science, Massachusetts Institute of Technology, Cambridge, MA, USA. <sup>4</sup>Department of Mechanical and Process Engineering, Eidgenössische Technische Hochschule (ETH) Zürich, Zürich, Switzerland.

\*e-mail: [duan@bu.edu](mailto:duan@bu.edu)

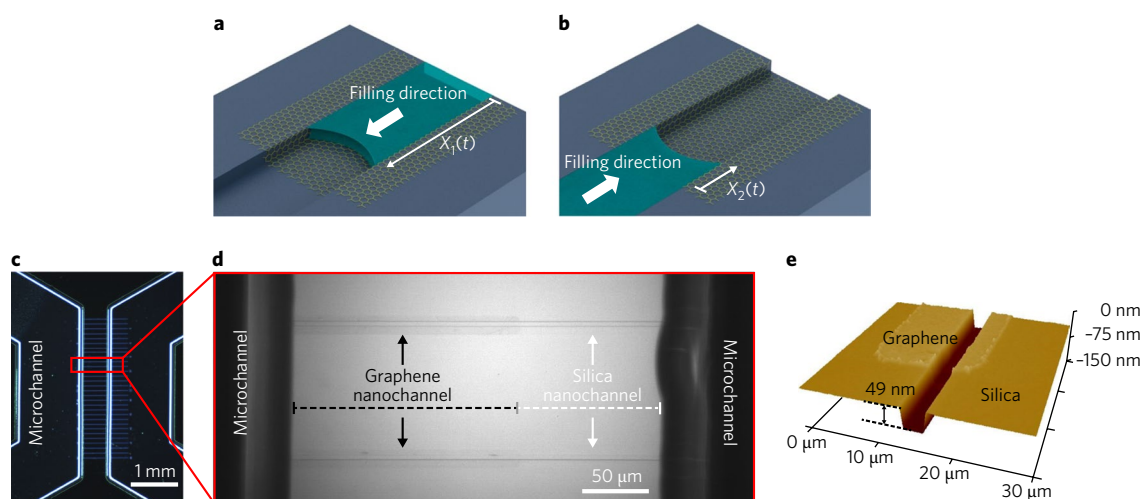


**Fig. 1 | Hybrid nanochannel design for water transport measurement in single graphene nanochannels.** **a, b**, Schematic of the hybrid nanochannel design. The graphene nanochannel to be studied is connected to a silica nanochannel with the same height and a known permeability. The capping layer of the nanochannel is not shown for clearer visualization. Water fills the graphene nanochannel from the graphene side and the capillary flow constant  $A$  is calculated based on the meniscus movement (**a**). Next, water fills the same graphene nanochannel from the silica side (**b**). The preceding silica nanochannel is filled before the meniscus arrives at the graphene nanochannel. The mass flow resistance ratio,  $\beta$ , between silica nanochannel and graphene nanochannel is calculated based on the meniscus movement in the graphene nanochannel and the capillary flow constant  $A$  extracted from the previous filling experiment. **c, d**, Microscope images of a fabricated hybrid nanochannel after anodic bonding. 30 nanochannels, which are  $100\text{ }\mu\text{m}$  apart, bridge two microchannels (**c**). A close view of **c** is shown in **d**. **e**, AFM characterization of a hybrid nanochannel before anodic bonding. The channel height for both the graphene nanochannel and silica nanochannel is  $49\text{ nm}$ . The roughness for the silica/graphene nanochannel area is  $0.47/0.98\text{ nm}$ .

Using this hybrid channel design, the capillary flow constant  $A$  can be determined by fitting the experimental data  $X_1(t)$  with equation (1). With  $A$  known, the mass flow resistance ratio  $\beta$  can be calculated by fitting the experimental data  $X_2(t)$  with equation (2). The flow resistance of the graphene nanochannel,  $R_G$ , can be consequently calculated, since the flow resistance of the silica nanochannel,  $R_S$ , is known (see error analysis in Supplementary Section 2 and ref. <sup>22</sup>). In contrast with previous capillary-filling measurements where the driving pressure is estimated either by the Young–Laplace equation or MD simulations, which may lead to significant inaccuracies<sup>5,17,23,24</sup>, our hybrid channel design enables accurate flow-resistance measurement without any theoretical estimations, which thus can unveil the true water slippage in graphene nanochannels.

Figure 1c shows a microscope image of one of the graphene-silica hybrid nanochannel devices used in this work. All the devices were fabricated using the aforementioned fabrication method, which involves nanochannel fabrication, graphene transfer and patterning as well as anodic bonding<sup>15</sup>. Each of these devices includes 30 nanochannels bridging two microchannels (Fig. 1c) and around 10 nanochannels will become hybrid graphene–silica nanochannels after graphene patterning. Clear optical contrast of the microscope image (Fig. 1d) allows for the lengths of graphene and silica nanochannels to be accurately measured.

The graphene nanochannels and the silica nanochannels have the same height and similar roughness (for example, in Fig. 1e,  $h = 49\text{ nm}$  and  $R_{\text{rms}} = 0.47/0.98\text{ nm}$  for the silica/graphene nanochannel). Overall, 24 devices with a wide range of channel heights, from 24 to  $124\text{ nm}$ , have been fabricated and tested. Capillary-filling measurements were conducted in these devices using de-ionized water (resistivity:  $18\text{ M}\Omega\text{-cm}$ ,  $\text{pH} = 6.2\text{--}6.4$  due to  $\text{CO}_2$  adsorption), and the menisci locations were tracked by a monochromatic high-speed camera (PHOTRON FASTCAM Mini UX50) mounted on an optical microscope (OLYMPUS BH2).

The menisci locations as a function of time during the two capillary-filling experiments were analysed with a MATLAB

image-processing code. Two typical results, one from a  $105\text{-nm}$  channel and the other from a  $25\text{-nm}$  channel are shown in Fig. 2a,b and Fig. 2c,d, respectively. Each capillary-filling process was plotted in two different colourmaps to better show the meniscus position and the corresponding fitting curve simultaneously. For both nanochannels, the first capillary-filling experiment started from the graphene side and the meniscus location  $X_1(t)$  inside the graphene nanochannel followed the Washburn's equation (equation (1)) and showed a clear parabolic trend (blue dotted lines in Fig. 2a,c) as a function of time.

In the second capillary-filling experiment, when water is introduced from the silica side, water flows through the silica nanochannel before entering the graphene nanochannel. Although the meniscus  $x$ – $t$  curve in the silica nanochannels can still be fitted using a parabolic curve (red dotted lines in Fig. 2b,d), it begins to deviate from the fitted parabola upon the meniscus reaching the graphene edge (the black dashed line) because the silica nanochannel and graphene nanochannel have different mass flow resistances and capillary driving pressures. The meniscus movement inside the graphene nanochannel (black dotted lines) could be either faster (Fig. 2b) or slower (Fig. 2d) than those in the silica nanochannels (red dotted lines). In certain cases (for example, Fig. 2d), a linear relation between the meniscus position and time is observed, indicating that the flow resistance mostly originates from the preceding silica channel and a large  $\beta$  should be expected. By fitting the different meniscus  $x$ – $t$  curves in the graphene nanochannel with equation (2) and using the capillary flow constant  $A$  extracted from the first filling experiment,  $\beta$  can be determined as 1.6 and 4.0 for the  $105\text{-}$  and  $25\text{-nm}$  nanochannels, respectively.

We performed similar experiments and analyses for all graphene–silica hybrid nanochannels of all 24 devices where the moving menisci can be clearly determined (Supplementary Section 3). The extracted mass flow resistance ratio,  $\beta$ , is obtained as a function of the channel height for each device and plotted in Fig. 3a. Each column represents one device and each data point

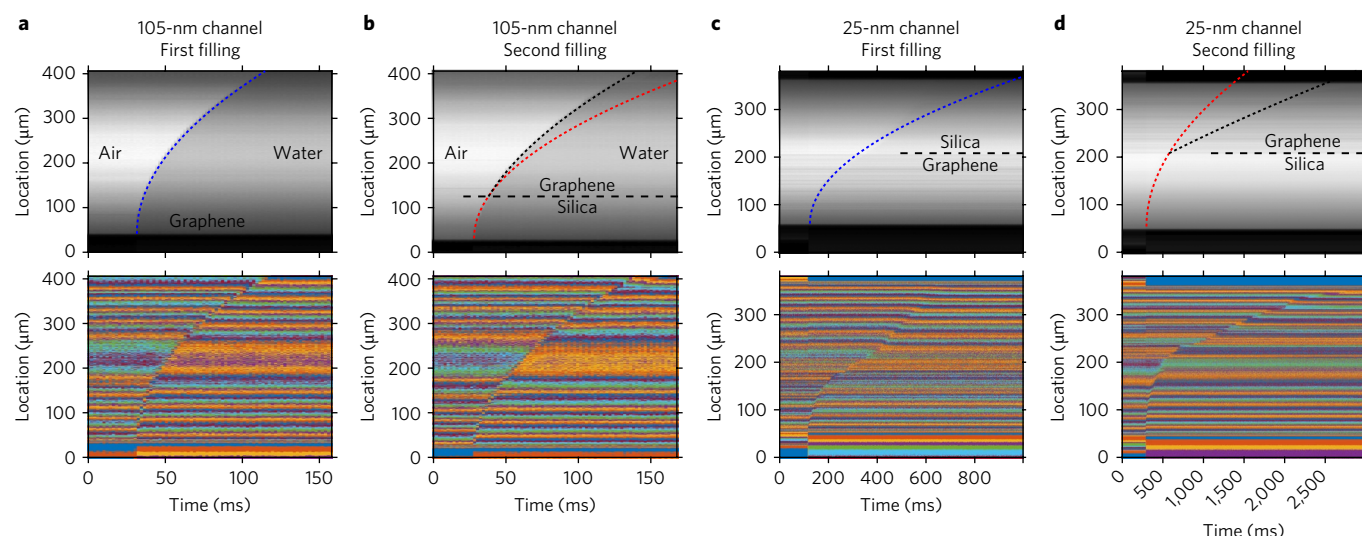


**Fig. 2 | Capillary-filling measurement in hybrid graphene-silica nanochannels.** **a,b**, Capillary-filling results of a 105-nm hybrid nanochannel. The bottom figures are replotted from the top figures with another colourmap for better visualization, as the meniscus is very difficult to trace in shallow channels. Meniscus location as a function of time in the first capillary-filling experiment of the 105-nm nanochannel which starts from the graphene side,  $X_1(t)$ , follows a parabolic trend (the blue dotted line). The capillary flow constant,  $A$ , can be extracted from the best fit (**a**). Meniscus location as a function of time in the second experiment of the 105-nm nanochannel which starts from the silica side (**b**). The red dotted line corresponds to the meniscus movement in the preceding silica nanochannel, and the black dotted line corresponds to the meniscus movement after entering the graphene nanochannel,  $X_2(t)$ , which deviates from the red dotted line. The mass flow resistance ratio,  $\beta$ , can be determined from the capillary flow constant,  $A$ , and the best fit (the black dotted line). The black dashed line in **b** represents the edge of graphene inside the nanochannel. **c,d**, Meniscus location as a function of time for a 25-nm hybrid nanochannel in the first (**c**) and second (**d**) capillary-filling experiment.

represents one hybrid nanochannel. Our results show that  $\beta$  varies between 0.5 and 4.0 for our graphene nanochannels and there is no clear correlation between the flow resistance ratio and the channel height. In fact,  $\beta$  can drastically change even for the same channel height.

Such variation in the mass flow resistance ratio  $\beta$  is not expected. If we assume that the quality and coverage of graphene inside the channel is perfect for all our measured hybrid nanochannel devices, the observed flow enhancement should be attributed to the slippage inside our graphene nanochannels. Based on the Navier–Stokes equation (Supplementary Section 4), the mass flow resistance ratio in the hybrid nanochannel can be derived as:

$$\beta_0 = \frac{R_S}{R_G} = \frac{\eta_S}{\eta_G} \frac{\rho_G}{\rho_S} \frac{w_G}{w_S} \left( \frac{h_G}{h_S} \right)^3 \frac{1 + \frac{4L_{\text{slip,G}}}{h_G}}{1 + \frac{L_{\text{slip,G}}}{h_G}} \quad (3)$$

Where  $\eta$  is the water viscosity and  $L_{\text{slip,G}}$  is the water slip length at the graphene surface. All variables with subscript G correspond to the properties in the graphene nanochannel, whereas the variables with subscript S represent the properties in the silica nanochannel. If the average fluid properties (density and viscosity) are the same in both graphene and silica nanochannels<sup>22,25–27</sup>, the mass flow resistance ratio is only related to the nanochannel geometry and the water slip length,  $L_{\text{slip,G}}$ . Consequently, it is expected that the mass flow resistance ratio would slightly increase with decreasing channel height for a constant graphene slip length (see grey bar plot in Fig. 3a) and have a minimum value of 1 in the case of  $L_{\text{slip,G}} = 0$ . The fact that some of our measured mass flow resistance ratios ( $\beta$ ) are less than one thus suggests that the graphene quality and coverage are not perfect in the graphene nanochannels investigated in this study and the measured mass flow resistance ratios ( $\beta$ ) may not correspond to those graphene nanochannels with full coverage of three-side graphene<sup>19</sup>. This indicates that our

fabrication method may not guarantee perfect graphene coverage and quality inside the graphene nanochannels especially for those deep channels although 25-nm graphene nanochannels prepared by this method have shown good coverage and quality<sup>15</sup>. In fact, incomplete coverage, scratch/crumpled graphene, and left-over polymer residues can be observed under the microscope in some of the graphene nanochannels deeper than 30 nm (Supplementary Section 5) although most areas within the channel appear to be uniform. We hypothesize that these coverage/quality issues are mainly associated with fatigue cracks during the graphene nanochannel fabrication<sup>28</sup> and deeper nanochannels are more prone to have such fatigue-crack related issues as the greater height-to-width ratios of these nanochannels would lead to higher stress at the structure edges during the drying/baking process of graphene transfer. This hypothesis has been confirmed by Raman spectroscopy mapping of our graphene nanochannels (see Supplementary Section 6). Furthermore, the Raman spectroscopy mapping demonstrates that channels with poor graphene coverage/quality are always associated with low mass flow resistance ratios ( $\beta < 1$ ) (Supplementary Sections 6 and 7), suggesting that the flow impediment is contributed by the coverage/quality issues in our graphene nanochannels.

### Capillary pressure inside the graphene nanochannels

Since such bad coverage and quality of graphene should directly affect the graphene surface energy and change the capillary driving pressure of the graphene nanochannel, we extracted the capillary pressure  $\Delta P_G$  of all graphene nanochannels based on equation (2) and correlated them with the mass flow resistance ratio in Fig. 3b. The capillary pressure is normalized with a pressure based on the Young–Laplace equation ( $\Delta P_0 = 2\gamma/h$ ). According to our data, the shallower channels tend to have smaller  $\Delta P_G$  and greater  $\beta$  while deeper channels show greater  $\Delta P_G$  and smaller  $\beta$ . This resonates well with our previous hypothesis of graphene quality/coverage in graphene nanochannels.

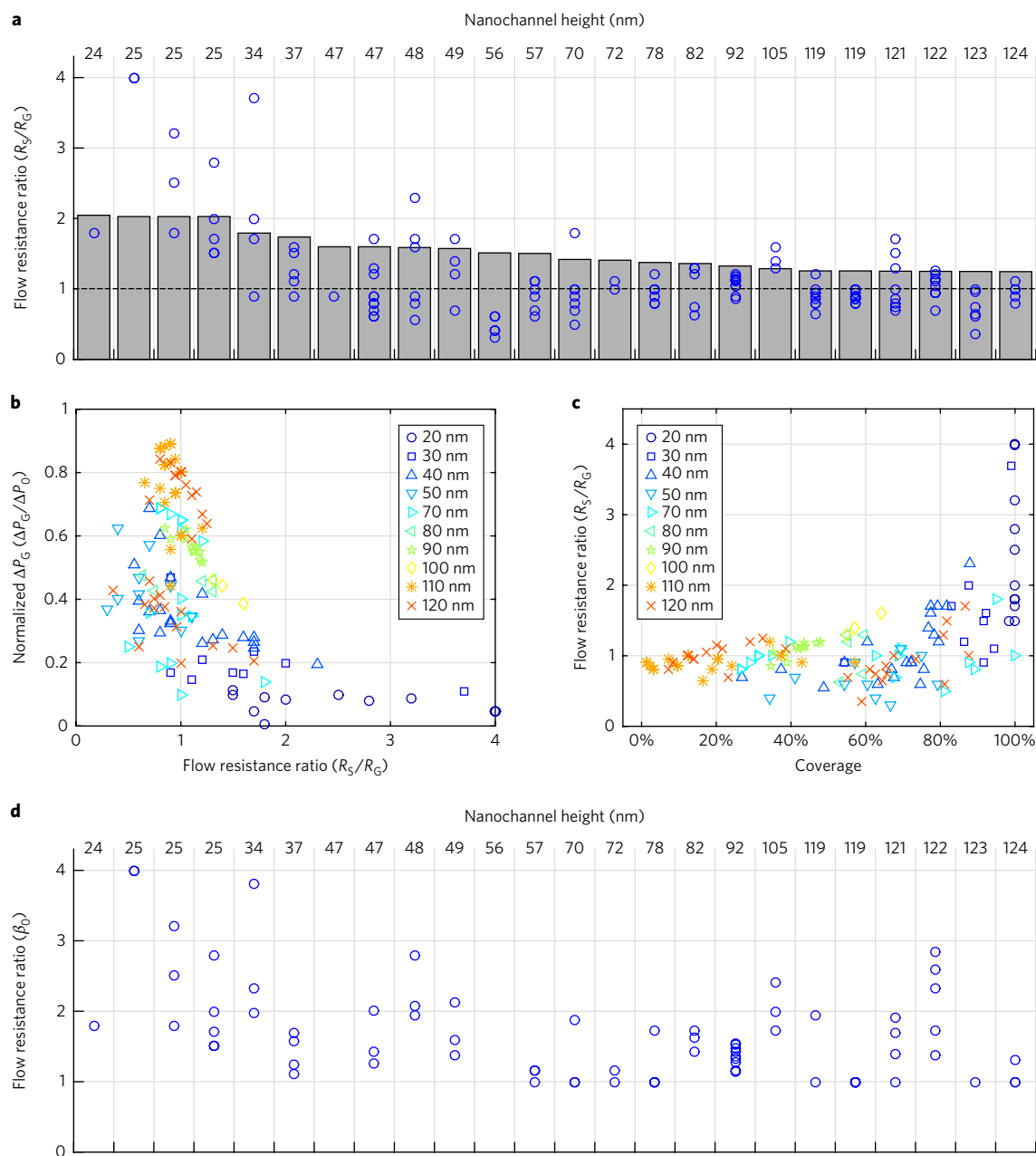


**Fig. 3 | Experimental mass flow resistance ratio in hybrid nanochannels with heights varying from 24 to 124 nm. a**, The extracted mass flow resistance ratio,  $\beta$ , for each individual hybrid nanochannel. Heights of the nanochannels are marked on the top. The grey bar plot shows the ratio calculated from equation (3) by assuming a constant slip length of 10 nm at the graphene surface. **b**, The normalized extracted capillary pressure  $\Delta P_G$  versus  $\beta$ . Each symbol represents channels with a certain range of heights, for example the ‘30 nm’ data marked with blue squares include data from 34- and 37-nm hybrid nanochannels shown in **a**. **c**, The extracted  $\beta$  versus graphene coverage calculated from equation (5). **d**, Extracted  $\beta_0$  considering partial graphene coverage for individual hybrid nanochannels with  $\beta > 1$ .

Theoretically, from the viewpoint of surface energy<sup>29</sup>, the capillary pressure in our graphene nanochannel can be expressed as:

$$\Delta P_G = \frac{c\Delta P_{\text{Graphene}} + (1-c)\Delta P_{\text{SiO}_2} + \Delta P_{\text{SiO}_2}}{2} \quad (4)$$

Here  $c$  represents the effective coverage of graphene on the channel floor ( $0 \leq c \leq 1$ ),  $\Delta P_{\text{Graphene}}$  is the effective capillary pressure inside the fully graphene-covered channel (both the ceiling and the floor of the nanochannel are covered with high quality graphene), and  $\Delta P_{\text{SiO}_2}$  is the capillary pressure inside the silica channel (Supplementary

Section 8). Based on this equation, we can estimate the effective graphene coverage using the measured capillary pressure. This capillary-pressure-based coverage analysis is time efficient and closely associated with the capillary flow inside the nanochannel, and its validity is confirmed by a good agreement with Raman spectroscopy mapping (Supplementary Section 9).

Figure 3c shows the correlation between the estimated graphene coverage ( $c$ ) and the measured mass flow resistance ratio ( $\beta$ ) for all our graphene nanochannels. Most of the graphene nanochannels with  $\beta$  less than 1 have graphene coverage less than 60%. This further strengthens our earlier observation that the measured flow impediment ( $\beta < 1$ ) comes from the bad quality and coverage



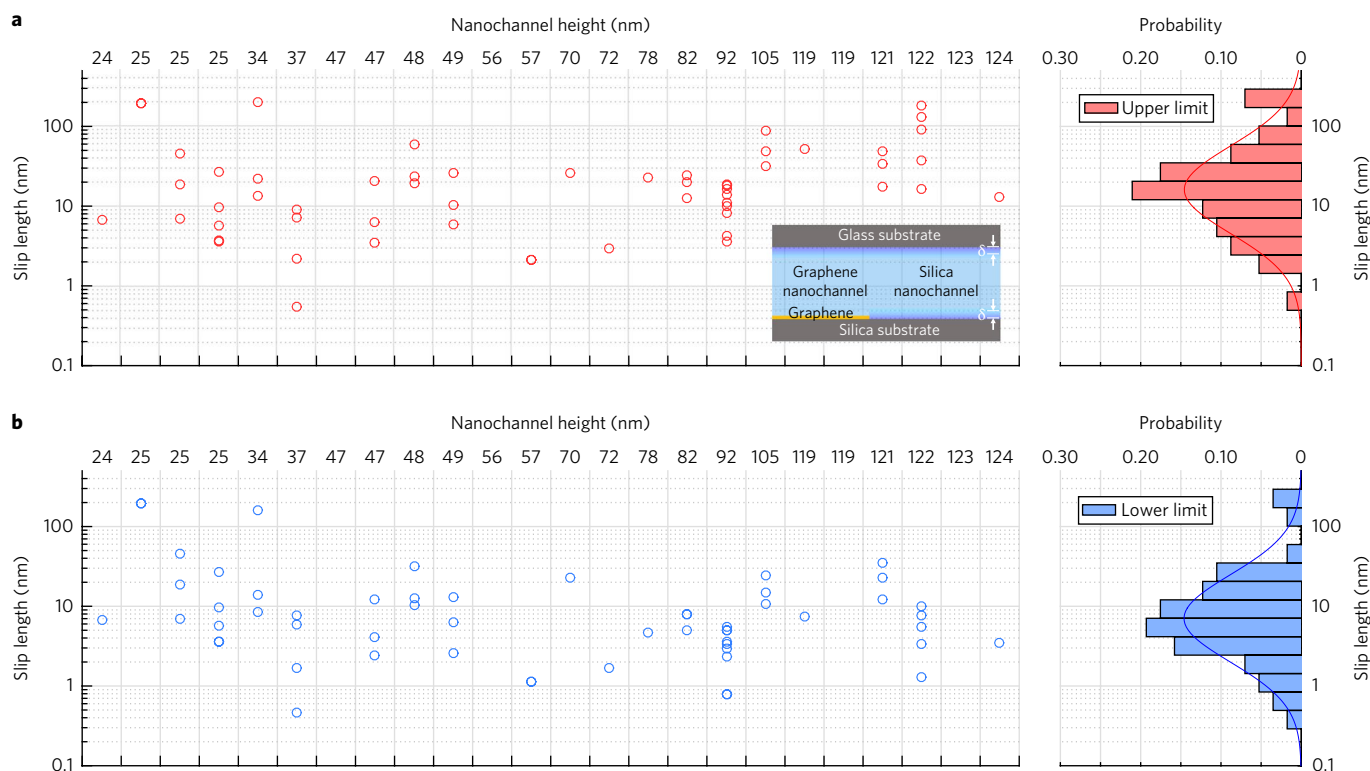


**Fig. 4 | The extracted slip length ( $L_{\text{slip,G}}$ ) based on equation (3) for each individual hybrid nanochannel with  $\beta_0$  greater than 1. **a**, The extracted slip length ( $L_{\text{slip,G}}$ ) considering graphene coverage/quality in the nanochannel. Height of the nanochannels are marked on the top. The histogram on the right shows that the extracted slip length follows a lognormal distribution with the statistical median of 16 nm. This analysis may overestimate the actual slip length and thus is labelled as ‘upper limit’. **b**, The extracted slip length ( $L_{\text{slip,G}}$ ) without considering graphene coverage/quality in the nanochannel. The complete graphene coverage is assumed for all the tested channels. Histogram on the right shows the lognormal distribution of extracted slip length with the statistical median of 7 nm. This analysis underestimates the actual slip length and will give us a ‘lower limit’ of the actual slip length.**

of graphene inside the channels. Consequently, these data cannot reflect the true water slippage of the graphene surface and thus we only focus on results from the graphene nanochannels with mass flow resistance ratios greater than 1.

Considering the partial coverage, the mass flow resistance ratio  $\beta_0$  for complete graphene coverage can be correlated with the measured flow resistance ratio  $\beta$  based on the relation of resistances in series:

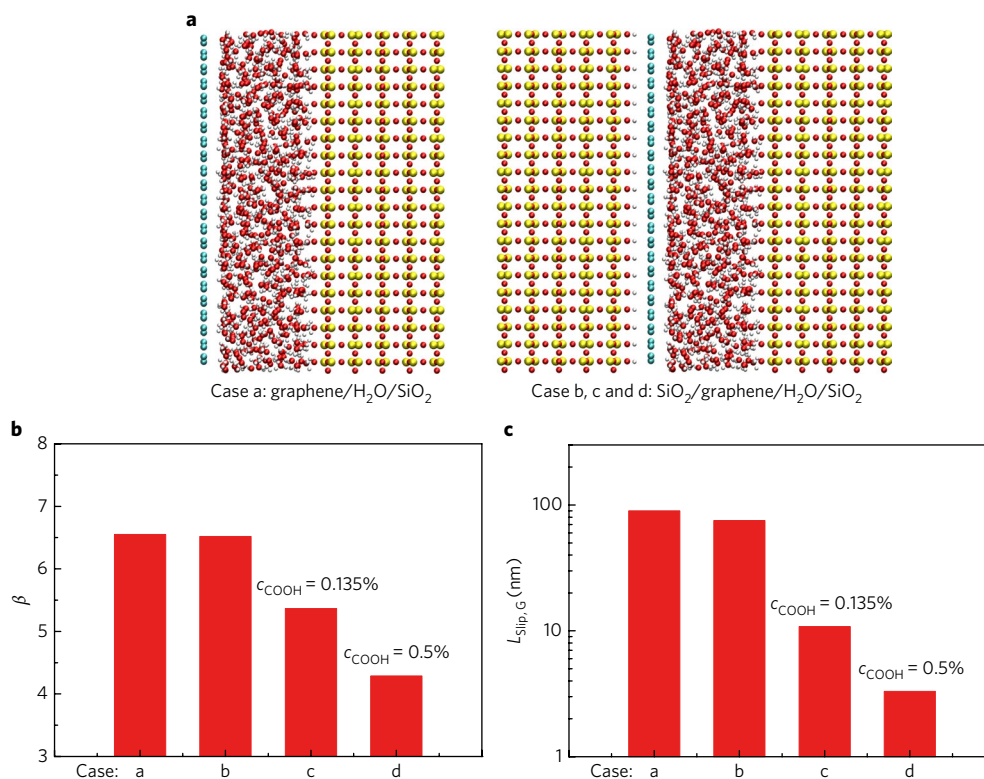
$$1/\beta = c/\beta_0 + 1 - c \quad (5)$$

Figure 3d plots the experimentally extracted flow resistance ratio  $\beta_0$  for each graphene nanochannel, which still does not show specific height dependence and has values between 1 and 4.

### Slip length of the graphene surface

Based on equations (3) and (5), the slip length of the graphene surface for each individual nanochannel is calculated and results are presented in Fig. 4a. The nanochannel heights are adjusted according to the presence of the immobilized hydration layer on silica surfaces<sup>22,24,30–32</sup> (inset of Fig. 4a). The extracted slip length spans two orders of magnitude from 0 to 200 nm and does not show any obvious dependence on the channel height. In addition, the extracted slip length seems to follow a lognormal distribution ( $L_{\text{slip,G}} \sim \text{lognormal}(\mu, \sigma^2)$ ) well and the statistical median is 16 nm. Since we assume that the nanochannel surface is either plain silica or perfect-quality graphene in our coverage analysis, it is possible that our analysis underestimates the actual graphene coverage because the graphene could be bad quality and have less capillary driving pressure. As a result, the calculated slip length (shown in

Fig. 4a) may overestimate the actual slip length of the graphene. Therefore, to find the lower bound of the slip length, we repeated the calculations this time based on the assumption of full graphene coverage for all channels, which ignores all possible flow impediment induced by graphene imperfections. The results are presented in Fig. 4b. The slip length calculated based on the assumption of full coverage still shows a large variation of values, between 0 and 200 nm, with a statistical median of 7 nm. In addition to this conservative approach, we also examined the slip length of nanochannels with more than 90% graphene coverage (see Supplementary Section 10) where the additional water flow impediment due to incomplete coverage is negligible and observed a similar range of variation. Therefore, we believe that the small, yet widely varying values of the graphene slip length are true characteristics of water slippage in the graphene nanochannels. The extracted statistical median of the measured slip length ( $L_{\text{slip,G}} = 16$  nm) is smaller than what has been estimated in graphene capillaries made of pristine multilayered graphene ( $L_{\text{slip,G}} = 60$  nm)<sup>5</sup>, but is actually quite close to the reported slip length of a single CNT with a diameter of 50 nm ( $L_{\text{slip,G}} = 17$  nm)<sup>33</sup>, where the curvature effect is relatively small. Since there is a large difference between the reported surface charge density,  $\sigma$ , in these two previous studies ( $\sigma \approx 0.05$  mC m<sup>-2</sup> in ref. 5 and  $\sigma \approx 5$  mC m<sup>-2</sup> in refs. 18,33), we hypothesize that the observed variation of the graphene slip length is due to the functional groups and charges on the graphene surface. According to our ion transport study in graphene nanochannels and several recent studies of graphene electrochemistry from other groups, the graphene made from the CVD process has certain surface charges<sup>15,34–37</sup>. The corresponding surface charge density is found to be insensitive to the effective ion concentration and pH at low salt concentrations<sup>15</sup>, suggesting



**Fig. 5 | MD simulations of water slippage in graphene nanochannels.** **a**, Simulation snapshots that illustrate the molecular models of water confined between graphene (with or without the silica substrate) and silica. **b, c**, The flow resistance ratio  $\beta$  (**b**) and slip length  $L_{\text{slip,G}}$  (**c**) calculated from our MD simulation results. For the oxidized graphene, we consider the relative surface density of carboxyl groups, that is, the ratio between the number of carboxyl groups and that of carbon atoms in graphene,  $c_{\text{COOH}} = 0.135\%$  and  $0.5\%$ , respectively.

that it may be only related to the graphene properties themselves (Supplementary Section 11). The presence of such surface charges could decrease the smoothness of a potential energy landscape as well as the hydrophobic nature of the graphene surface, consequently reducing the flow slippage. In addition to surface charges, the underlying silica substrate may also contribute to the decrease of the flow slippage, as the interaction between water molecules and this polar hydrophilic substrate cannot be totally screened by the single-layer graphene<sup>38–40</sup>.

### MD simulation of substrate and surface charge effects

To further confirm these two effects, we performed MD simulations using typical parameters for water–water and water–carbon interactions for graphene nanochannels ( $h = 1.8$  nm) with four different types of graphene surface (Methods and Supplementary Section 12): (a) pristine graphene without silica substrate underneath; (b) pristine graphene in intimate contact with the silica substrate underneath; (c) graphene oxide surface (graphene surface with 0.135% randomly distributed carboxyl groups) in intimate contact with the silica substrate underneath; and (d) graphene oxide surface (graphene surface with 0.5% randomly distributed carboxyl groups) in intimate contact with the silica substrate underneath (Fig. 5a). The surface occupancy of carboxyl groups in (c) and (d) were chosen, respectively, in accordance with the average surface charge density ( $8 \text{ mC m}^{-2}$ ) measured in our previous graphene nanochannel ion transport study<sup>15</sup> and the maximum surface charge density reported in literature ( $32 \text{ mC m}^{-2}$ )<sup>35</sup>.

The flow resistance ratios in these four cases are 6.55, 6.52, 5.37 and 4.29 corresponding to graphene slip lengths of 90.0, 75.2, 10.8 and 3.3 nm. The calculated flow resistance ratios are greater than the maximum theoretical prediction of equation (3) perhaps because the MD simulation results indicate that even a bare silica

surface has a finite slip length of 0.4 nm, which is not consistent with our previous experimental water transport study of silica nanochannels<sup>22</sup>. Nevertheless, it is clear from the MD simulation that the nanochannels with graphene surface (c) and (d) yield the smallest flow enhancement and slip length, which are followed by the nanochannel with graphene surface (b), and then the nanochannel with graphene surface (a). Furthermore, higher coverage of functional groups and thus higher surface charge densities tend to further decrease the flow enhancement and slippage of graphene surface. It is worth mentioning that slip length in case (c) ( $L_{\text{slip,G}} = 10.8$  nm) is actually in agreement with the statistical median of extracted slip length, proving that the surface charge and underneath substrate can indeed affect the slip length of graphene significantly.

The effects of graphene surface charge and the underlying silica substrate can also explain the large variation of the extracted slip length. We notice that surface charge densities of graphene can vary from nearly 0 to  $32 \text{ mC m}^{-2}$  (corresponding to  $\sim 0.5\%$  coverage of carboxyl groups) according to several recent studies and our investigation of ion transport in graphene nanochannels<sup>15,34–37</sup>. We also notice that not all the transferred graphene has perfect intimate contacts with the underlying silica substrate—AFM images show that in certain cases the apparent height difference between graphene and the surrounding silica substrate could be as large as 5 nm (Supplementary Section 13) despite  $\sim 0.3$  nm of the graphene thickness. This varying gap size can alter the substrate interaction effect and give rise to variations in the slip length. The observed ultra-small slip length (for example, less than 5 nm) likely corresponds to a graphene surface with large surface charge density induced by surface functional groups and intimate contact (a strong interaction) with the silica surface (case d). In contrast, the observed large slip length (for example, 200 nm) would most likely correspond to a graphene surface with negligible surface charge density and

weak interaction with the silica substrate (case a). In other words, it is conceivable that the slip length of pristine graphene could be close to or even greater than 200 nm, which is still greater than the measured slip length of graphite<sup>41</sup> and most MD simulation predictions<sup>42–44</sup> and thus is worthy of further investigation.

## Conclusions

In conclusion, our hybrid-nanochannel-based capillary-filling measurements allow us to unambiguously measure water transport in single graphene nanochannels and extract the slip length of planar graphene even in cases of imperfect graphene coverage and quality. Our results advance understanding of water transport in carbon nanofluidics and indicate that the graphene surface charge and the substrate effect could significantly influence the slip length of graphene. We expect this method will also enable investigation of water transport in other graphitic conduits including single CNTs and graphene nanopores as well as in single biological channels such as aquaporins if more sensitive approaches of tracing the meniscus (for example, electrical methods) and precise fabrication methods of connecting the target conduit with a reference conduit are implemented.

## Methods

Methods, including statements of data availability and any associated accession codes and references, are available at <https://doi.org/10.1038/s41565-017-0031-9>.

Received: 9 March 2017; Accepted: 17 November 2017;

Published online: 1 January 2018

## References

- Majumder, M., Chopra, N., Andrews, R. & Hinds, B. J. Nanoscale hydrodynamics: enhanced flow in carbon nanotubes. *Nature* **438**, 44 (2005).
- Holt, J. K. et al. Fast mass transport through sub-2-nanometer carbon nanotubes. *Science* **312**, 1034–1037 (2006).
- Nair, R. R., Wu, H. A., Jayaram, P. N., Grigorieva, I. V. & Geim, A. K. Unimpeded permeation of water through helium-leak-tight graphene-based membranes. *Science* **335**, 442–444 (2012).
- Huang, H. et al. Ultrafast viscous water flow through nanostrand-channelled graphene oxide membranes. *Nat. Commun.* **4**, 2979 (2013).
- Radha, B. et al. Molecular transport through capillaries made with atomic-scale precision. *Nature* **538**, 222–225 (2016).
- Corry, B. Designing carbon nanotube membranes for efficient water desalination. *J. Phys. Chem. B* **112**, 1427–1434 (2008).
- Das, R., Ali, M. E., Hamid, S. B. A., Ramakrishna, S. & Chowdhury, Z. Z. Carbon nanotube membranes for water purification: A bright future in water desalination. *Desalination* **336**, 97–109 (2014).
- Cohen-Tanugi, D. & Grossman, J. C. Water desalination across nanoporous graphene. *Nano Lett.* **12**, 3602–3608 (2012).
- Surwade, S. P. et al. Water desalination using nanoporous single-layer graphene. *Nat. Nanotech.* **10**, 459–464 (2015).
- Kim, H. W. et al. Selective gas transport through few-layered graphene and graphene oxide membranes. *Science* **342**, 91–95 (2013).
- Li, H. et al. Ultrathin, molecular-sieving graphene oxide membranes for selective hydrogen separation. *Science* **342**, 95–98 (2013).
- Joshi, R. K. et al. Precise and ultrafast molecular sieving through graphene oxide membranes. *Science* **343**, 752–754 (2014).
- Candelaria, S. L. et al. Nanostructured carbon for energy storage and conversion. *Nano Energy* **1**, 195–220 (2012).
- Park, H. G. & Jung, Y. Carbon nanofluidics of rapid water transport for energy applications. *Chem. Soc. Rev.* **43**, 565–576 (2014).
- Xie, Q., Xin, F., Park, H. G. & Duan, C. Ion transport in graphene nanofluidic channels. *Nanoscale* **8**, 19527–19535 (2016).
- Yongqiang, R. & Derek, S. Slip-enhanced electrokinetic energy conversion in nanofluidic channels. *Nanotechnology* **19**, 195707 (2008).
- Qin, X., Yuan, Q., Zhao, Y., Xie, S. & Liu, Z. Measurement of the rate of water translocation through carbon nanotubes. *Nano Lett.* **11**, 2173–2177 (2011).
- Secchi, E. et al. Massive radius-dependent flow slippage in carbon nanotubes. *Nature* **537**, 210–213 (2016).
- Wei, N., Peng, X. & Xu, Z. Understanding water permeation in graphene oxide membranes. *ACS Appl. Mater. Interfaces* **6**, 5877–5883 (2014).
- Boukhvalov, D. W., Katsnelson, M. I. & Son, Y.-W. Origin of anomalous water permeation through graphene oxide membrane. *Nano Lett.* **13**, 3930–3935 (2013).
- Muscattello, J., Jaeger, F., Matar, O. K. & Müller, E. A. Optimizing water transport through graphene-based membranes: insights from nonequilibrium molecular dynamics. *ACS Appl. Mater. Interfaces* **8**, 12330–12336 (2016).
- Alibakhshi, M. A., Xie, Q., Li, Y. & Duan, C. Accurate measurement of liquid transport through nanoscale conduits. *Sci. Rep.* **6**, 24936 (2016).
- Tas, N. R., Haneveld, J., Jansen, H. V., Elwenspoek, M. & van den Berg, A. Capillary filling speed of water in nanochannels. *Appl. Phys. Lett.* **85**, 3274–3276 (2004).
- Haneveld, J., Tas, N. R., Brunets, N., Jansen, H. V. & Elwenspoek, M. Capillary filling of sub-10nm nanochannels. *J. Appl. Phys.* **104**, 014309 (2008).
- Mortensen, N. A. & Kristensen, A. Electroviscous effects in capillary filling of nanochannels. *Appl. Phys. Lett.* **92**, 063110 (2008).
- Phan, V.-N., Yang, C. & Nguyen, N.-T. Analysis of capillary filling in nanochannels with electroviscous effects. *Microfluid. Nanofluid.* **7**, 519–530 (2009).
- Wang, M., Chang, C.-C. & Yang, R.-J. Electroviscous effects in nanofluidic channels. *J. Chem. Phys.* **132**, 024701 (2010).
- Hong, J.-Y. et al. A rational strategy for graphene transfer on substrates with rough features. *Adv. Mater.* **28**, 2382–2392 (2016).
- Huang, W., Liu, Q. & Li, Y. Capillary filling flows inside patterned-surface microchannels. *Chem. Eng. Technol.* **29**, 716–723 (2006).
- Sendner, C., Horinek, D., Bocquet, L. & Netz, R. R. Interfacial water at hydrophobic and hydrophilic surfaces: slip, viscosity, and diffusion. *Langmuir* **25**, 10768–10781 (2009).
- Goertz, M. P., Houston, J. E. & Zhu, X. Y. Hydrophilicity and the viscosity of interfacial water. *Langmuir* **23**, 5491–5497 (2007).
- Li, T.-D., Gao, J., Szoszkiewicz, R., Landman, U. & Riedo, E. Structured and viscous water in subnanometer gaps. *Phys. Rev. B* **75**, 115415 (2007).
- Secchi, E., Niguès, A., Jubin, L., Siria, A. & Bocquet, L. Scaling behavior for ionic transport and its fluctuations in individual carbon nanotubes. *Phys. Rev. Lett.* **116**, 154501 (2016).
- Ambrosi, A., Chua, C. K., Bonanni, A. & Pumera, M. Electrochemistry of graphene and related materials. *Chem. Rev.* **114**, 7150–7188 (2014).
- Ping, J. & Johnson, A. T. C. Quantifying the intrinsic surface charge density and charge-transfer resistance of the graphene-solution interface through bias-free low-level charge measurement. *Appl. Phys. Lett.* **109**, 013103 (2016).
- Chen, F., Qing, Q., Xia, J., Li, J. & Tao, N. Electrochemical gate-controlled charge transport in graphene in ionic liquid and aqueous solution. *J. Am. Chem. Soc.* **131**, 9908–9909 (2009).
- Zhong, J.-H. et al. Quantitative correlation between defect density and heterogeneous electron transfer rate of single layer graphene. *J. Am. Chem. Soc.* **136**, 16609–16617 (2014).
- Rafiee, J. et al. Wetting transparency of graphene. *Nat. Mater.* **11**, 217–222 (2012).
- Shih, C.-J. et al. Breakdown in the wetting transparency of graphene. *Phys. Rev. Lett.* **109**, 176101 (2012).
- Shih, C.-J., Strano, M. S. & Blankschtein, D. Wetting translucency of graphene. *Nat. Mater.* **12**, 866–869 (2013).
- Maali, A., Cohen-Bouhacina, T. & Kellay, H. Measurement of the slip length of water flow on graphite surface. *Appl. Phys. Lett.* **92**, 053101 (2008).
- Thomas, J. A. & McGaughey, A. J. H. Reassessing fast water transport through carbon nanotubes. *Nano Lett.* **8**, 2788–2793 (2008).
- Kumar Kannam, S., Todd, B. D., Hansen, J. S. & Davis, P. J. Slip length of water on graphene: limitations of non-equilibrium molecular dynamics simulations. *J. Chem. Phys.* **136**, 024705 (2012).
- Falk, K., Sedlmeier, F., Joly, L., Netz, R. R. & Bocquet, L. Molecular origin of fast water transport in carbon nanotube membranes: superlubricity versus curvature dependent friction. *Nano Lett.* **10**, 4067–4073 (2010).

## Acknowledgements

This work is supported by the Faculty Startup Fund (Boston University, USA) and the NSF Faculty Early Career Development (CAREER) programme award (CBET-1653767). The authors would like to thank the Photonics Center at Boston University for the use of their fabrication and characterization facilities. S.J. and Z.X. acknowledge the support from the National Natural Science Foundation of China through grant no. 11472150. M.H. and J.K. are thankful for financial support by the AFOSR FATE MURI, grant no.

FA9550-15-1-0514. H.G.P. appreciates the support from ETH grant (ETH-30 13-1) and Swiss National Science Foundation (200021-146856).

### Author contributions

C.D. conceived the idea and directed the project; C.D., Q.X. and M.A. designed the experiments; Q.X. fabricated the nanofluidic devices and performed the experiments; Q.X. and M.A. analysed the experimental data; S.J. and Z.X. performed the MD simulations; M.H., J.K. and H.G.P. provided graphene samples; C.D., Q.X. and Z.X. wrote the manuscript. All authors participated in completing the manuscript.

### Competing interests

The authors declare no competing financial interests.

### Additional information

**Supplementary information** is available for this paper at <https://doi.org/10.1038/s41565-017-0031-9>.

**Reprints and permissions information** is available at [www.nature.com/reprints](http://www.nature.com/reprints).

**Correspondence and requests for materials** should be addressed to C.D.

**Publisher's note:** Springer Nature remains neutral with regard to jurisdictional claims in published maps and institutional affiliations



## Methods

**Device fabrication.** The silica nanochannels were first fabricated with optical photolithography and controlled reactive ion etching ( $\text{CF}_4$ ) on a silicon substrate. Subsequently, 280-nm-thick silicon oxide was thermally grown on the silicon substrate to ensure the surface hydrophilicity, improve the optical contrast and facilitate the anodic bonding. CVD graphene was then transferred from copper foil to the substrate with patterned open nanochannels via a PMMA-assisted wet transfer method. Due to small height-to-width ratio of the open nanochannels, the transferred graphene covered the substrate conformally. Afterwards, the graphene was patterned into different lengths (shorter than the nanochannel), forming silica-graphene hybrid nanochannels on the substrate. After annealing the device under an  $\text{Ar}/\text{H}_2$  environment, the substrate was bonded with another glass substrate containing access microchannels and reservoirs. The anodic bonding process (800 V, 450 °C) was performed under vacuum ( $\sim 10^{-4}$  Torr) to ensure the survival of graphene inside the enclosed nanochannel.

**Molecular dynamics simulations.** Molecular dynamics (MD) simulations are performed by using the large-scale atomic/molecular massively parallel simulation (LAMMPS)<sup>45</sup>. The all-atom optimized potentials for liquid simulations (OPLS-AA) force field is used to construct atomic models of graphene and graphene oxide<sup>46</sup>. We constructed carboxyl-functionalized graphene (on both sides of the sheet) with various concentrations. The SPC/E model<sup>44,47</sup> is used for water with the SHAKE algorithm, which predicts the density and viscosity of bulk water as  $0.9913 \text{ kg l}^{-1}$  and  $0.729 \text{ mPa s}$ . The van der Waals interaction between water and graphene is described following the Lennard-Jones 12–6 form, that is  $V = 4\epsilon[(\sigma/r)^{12} - (\sigma/r)^6]$ , where  $r$  is the interatomic distance between oxygen and carbon atoms. Parameters  $\epsilon = 0.09365 \text{ kcal mol}^{-1}$  and  $\sigma = 0.3190 \text{ nm}$  are chosen, yielding a water contact angle

of  $95^\circ$  on graphene<sup>48</sup>. The silica surfaces are created by cutting the cristobalite by its (111) surface that consists of low-density ( $4.54 \text{ -OH nm}^{-2}$ ) hydroxyl groups. The CLAYFF force field is used for  $\text{SiO}_2$ . The Lorentz–Berthelot mixing rules are used for the van der Waals interactions between  $\text{SiO}_2$  and water molecules described in the Lennard–Jones 12–6 form. The van der Waals forces are truncated at 1.2 nm and long-range Columbic interactions are computed using the particle–particle particle–mesh (PPPM) algorithm<sup>48</sup>. A time step of 1.0 fs is used to integrate the equations of motion. The total time of simulation is a few nanoseconds. Water molecules are equilibrated at 300 K using the Berendsen thermostat. More details are provided in Supplementary Section 12.

**Data availability.** The data that support the plots within this paper and other findings of this study are available from the corresponding author upon reasonable request.

## References

45. Plimpton, S. Fast parallel algorithms for short-range molecular dynamics. *J. Comput. Phys.* **117**, 1–19 (1995).
46. Shih, C.-J., Lin, S., Sharma, R., Strano, M. S. & Blankschtein, D. Understanding the pH-dependent behavior of graphene oxide aqueous solutions: a comparative experimental and molecular dynamics simulation study. *Langmuir* **28**, 235–241 (2012).
47. Wei, N., Lv, C. & Xu, Z. Wetting of graphene oxide: a molecular dynamics study. *Langmuir* **30**, 3572–3578 (2014).
48. Hockney, R. W. & Eastwood, J. W. *Computer Simulation Using Particles* (Taylor & Francis, New York, 1988).